Quantitative and qualitative studies on high-contrast X-ray radiography with an asymmetrical crystal set-up at Elettra

Marcelo Gonçalves Hönnicke,[a]* Luigi Rigon,[b] Ralf-H. Menk[c] and Cesar Cusatis[a]

[a]LORXI, Departamento de Física, Universidade Federal do Paraná, Brazil, [b]Dipartamento di Fisica, Universitá di Trieste, Italy, and [c]Sincrotrone Trieste Scpa, Italy. E-mail: marcelo@fisica.ufpr.br

An analyzer-based X-ray phase contrast imaging (ABI) system with an asymmetrical crystal set-up was mounted at Elettra's SYRMEP beamline. It was the first time that this set-up was implemented at Elettra. Advantages and disadvantages of such a set-up were exploited with quantitative and qualitative studies. For quantitative studies a simple hollow tube and strands were used as samples. Qualitative studies were developed using this technique with ox brain tissue, which has never been previously examined in this manner. Minute details were found in the ABIs and in the diffraction enhanced images. This could indicate the possibility of using these techniques with computerized tomography in the future as an auxiliary method in diagnosing brain illnesses such as Alzheimer and Creutzfeldt-Jacob disease. Propagation-based X-ray phase contrast imaging was also qualitatively exploited and compared with ABI using a *Loxosceles gaucho* spider as a sample.

Keywords: X-ray imaging; phase contrast imaging; diffraction enhanced imaging; X-ray optics.

1. Introduction

X-ray images obtained using conventional radiography do not show details when the object (sample) under analysis has low attenuation contrast. Enhanced contrast imaging is achieved by exploiting the real part of the refraction index, which is responsible for the phase shifts, in addition to the imaginary part, which is responsible for the absorption. Such a technique is called X-ray phase contrast imaging. Three main techniques are reported in the literature for hard X-rays: interferometry (Ando & Hosoya, 1972), propagation-based X-ray phase contrast imaging (PBI) (Snigirev *et al.*, 1995; Wilkins *et al.*, 1996; Cloetens *et al.*, 1997) and analyzer-based X-ray phase contrast imaging (ABI) (Förster *et al.*, 1980; Podurets *et al.*, 1989; Ingal & Beliaevskaya, 1995; Davis *et al.*, 1995; Chapman *et al.*, 1997). Three types of contrast can be enhanced using ABI: extinction contrast (*i.e.* rejection of ultrasmall-angle X-ray scattering), refraction contrast and pure absorption contrast. The superposition of such effects can result in ambiguous interpretation (Pagot *et al.*, 2003) but this problem can be treated with appropriate mathematical image processing. The diffraction enhanced imaging (DEI) algorithm (Chapman *et al.*, 1997; Zhong *et al.*, 2000) separates refraction from apparent absorption (*i.e.* absorption and extinction) but neglects some effects owing to ultra-small-angle scattering. New mathematical methods for image processing that deal more specifically with ultra-small-angle scattering have been

introduced recently by Rigon *et al.* (2003), Pagot *et al.* (2003), Oltulu *et al.* (2003) and Wernick *et al.* (2003). Coan *et al.* (2005) and Pavlov *et al.* (2004) have also investigated the combination of ABI and PBI.

In the present investigation, quantitative and qualitative studies on ABI were carried out with an asymmetrical crystal set-up, at 17.4 keV, mounted at the SYRMEP beamline of Elettra (Arfelli *et al.*, 1995) for the first time. For quantitative studies on ABI, a polypropylene tube and polyamide strands (segments of line) were used as samples. Several images were obtained at different angular positions on the rocking curve of the analyzer crystal. Measured cross-section profiles were compared with simulated ones both without any mathematical processing and after the application of the DEI algorithm (Chapman *et al.*, 1997).

Qualitative studies will be reported, for the first time, with a sample of ox brain tissue. The use of brain tissue with ABI has recently been applied to analysis of tumor in mouse models (Mannan *et al.*, 2005; Rigley *et al.*, 2005). Perhaps together with computed tomography, at higher energies, ABI could be useful as an alternative method for the diagnosis of brain illness without any use of contrast agents. The auxiliary methods currently used for diagnosis of brain diseases are: conventional computed tomography (CT), nuclear magnetic resonance (NMR), positron emission tomography (PET) and single-photon emission computed tomography (SPECT) where contrast agents are almost always used.

PBI data of a *Loxosceles gaucho* spider (violin spider) were acquired and qualitatively compared with an image obtained with the ABI.

The present report describes the experimental set-up, followed by quantitative and qualitative studies and conclusions.

2. Experiment

The experimental set-up is shown in Fig. 1. A double-crystal Si(111) monochromator upstream of the experimental hutch was used to select the energy at 17.4 keV. An asymmetrically cut Si(220) first crystal to expand the beam four times ($m = 4$) and a symmetrically cut Si(220) second crystal acting as a Bragg analyzer were used. To avoid strains these crystals were built with strain releases. The beam size on the sample was 20 mm × 16 mm. Both crystals were mounted, independently of the beamline monochromator, on a double-axis diffractometer, similar to that built by Hart (1980), to assure thermomechanical stability. The theoretical rocking-curve width of the analyzer crystal is 5 µrad, but the measured width was 12 µrad because, even using strain releases, the large analyzer crystal (120 mm in length) was slightly bent by its own weight. The main advantage of using asymmetrically cut crystals is that the laminar beam is expanded in the vertical plane and subsequently the field of view in this direction is magnified. For small samples this set-up does not require the simultaneous translation of sample and detector, which typically introduces blurring artifacts. Therefore this set-up enables high-resolution imaging in the vertical direction. However, such a set-up requires large strain-free analyzer crystals and implies a loss of the beam coherence owing to the energy dispersion in asymmetrically cut crystals (Souvorov *et al.*, 1999).

The samples were placed between the two crystals. Images were acquired at different angular positions on the rocking curve (Fig. 2) of the analyzer crystal. Images were also obtained from refraction angle and apparent absorption contrast by means of the DEI mathematical processing (Chapman *et al.*, 1997). Conventional synchrotron radiographs were acquired by placing the samples beyond the crystals, in contact with the detector.
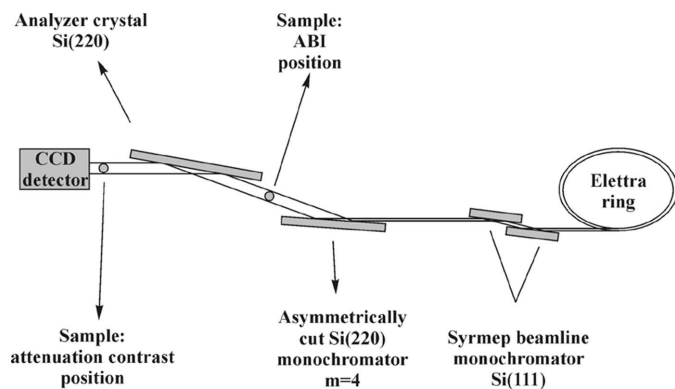
The small vertical source size of the Elettra machine at the SYRMEP beamline (100 µm) coupled with the distance from the source to the sample (25 m) and a high-spatial-resolution CCD detector made it possible to acquire images of thick samples using the PBI method in the edge detection geometry. Such images are acquired setting the sample just after the crystals and far from the detector.

All images were acquired using a CCD detector with 2048 × 2048 pixels (each one measuring 14 µm × 14 µm) with magnifying optics (40:11 taper) that gives a theoretical pixel size of 3.5 µm × 3.5 µm. The spatial resolution of this detector will be discussed in the next section.

3. Quantitative studies

A polypropylene hollow tube with an external diameter of 6 mm and internal diameter of 3.8 mm was used. This tube was fixed on a one-layer paper matrix (about 50 µm thick) so that the polypropylene tube combines refraction and absorption effects while the paper exhibits mainly the extinction effect (Oltulu *et al.*, 2003). Other samples used were polyamide strands with two different diameters, 100 µm and 250 µm.

Images of the polypropylene tube and of the polyamide strands are shown in Figs. 3 and 5. Fig. 3 shows images of a detail (bottom half) of the polypropylene tube. As expected, the tube edges and the cluster of the paper fibers are poorly seen using conventional synchrotron radiography (Fig. 3a) while they are enhanced and clearly identified in the ABI obtained at an angular position corresponding to the top of the rocking curve (Fig. 3b). An ABI acquired at the angular position at the top of the rocking curve shows contrast arising

Figure 1
Analyzer-based X-ray phase contrast imaging set-up at the SYRMEP beamline of Elettra at 17.4 keV. The monochromator immediately before the sample is an asymmetrically cut Si(220) crystal for magnifying the incoming beam four times ($m = 4$).
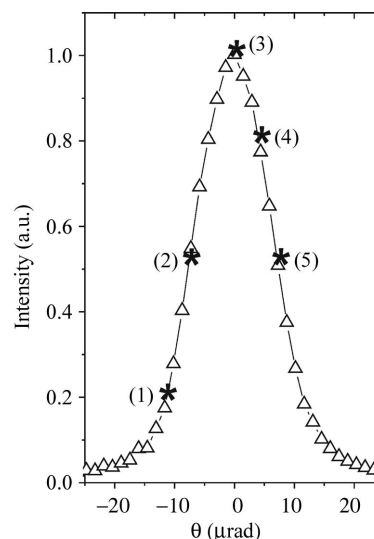
Figure 2
Rocking curve of the Si(220) analyzer crystal, at 17.4 keV. The angular positions where the images of the next figures were acquired are indicated by the numbers (1)–(5).

from ultra-small-angle X-ray scattering (extinction), refraction and pure absorption. ABIs acquired on the slopes on the rocking curve (Figs. 3*c* and 3*d*) also show much sharper contrast than the conventional synchrotron radiography. The contrast is inverted for the images acquired at angular positions corresponding to the opposite slope on the rocking curve (positions 2 and 5 in Fig. 2) and the cluster of the paper fibers is not so clearly seen as in the image acquired at the top angular position. Hence these images can be used to obtain refraction angle and apparent absorption contrast images (DEIs). The apparent absorption contrast images are scatter-free and only absorption and extinction produce the contrast, *i.e.* the image in Fig. 3(*e*) clearly shows the cluster of the paper fibers (extinction contrast) and the absorption profile of the polypropylene tube. Finally, the refraction angle images represent the spatial gradient of the refractive index (Chapman *et al.*, 1997) as shown in the image in Fig. 3(*f*).

Measured and simulated cross-section profiles of the images were obtained in order to understand the behavior of the images at different angular positions on the rocking curve of the analyzer crystal. The simulations, based on Snell's law, were performed considering a ray-tracing approach for an incoming monochromatic plane-wave beam being refracted and attenuated by the sample. The source size was considered as being punctual, *i.e.* with zero dimension. The rocking curve of the analyzer crystal was considered as a Gaussian profile of width 12 μrad and the theoretical pixel size used was 10 μm × 10 μm, approximately the spatial resolution of the acquired images. The same theoretical procedure has shown good agreement between the theoretical and experimental cross-sectional profiles when applied to these samples using lower energies, a low-spatial-resolution CCD detector (22.5 μm × 22.5 μm) and strain-free crystals (Hönnicke *et al.*, 2005). Also, these simulation procedures are similar to those used by Protopopov & Sobota (2002) using as analyzer a multilayer mirror with resonant absorption and conventional sources.

Measured and simulated cross-section profiles of the images of Fig. 3 are shown in Fig. 4. It can be seen that the contrast for the ABI images (Figs. 4*b*–4*d*) is about five times greater than for the contrast for conventional synchrotron radiography (Fig. 4*a*). It is also shown that the profile of images is inverted for opposite-slope angular positions on the rocking curve (Figs. 4*c* and 4*d*). The apparent absorption contrast image (Fig. 4*e*) shows a profile similar to the conventional synchrotron radiography except in the edges of the tube wall where strong refraction effects and subsequently extinction occurs. The refraction angle image (Fig. 4*f*) shows contrast twice as great as that of the ABI.

Fig. 5 shows ABIs of the polyamide strands where, once again, the edges are enhanced and the contrast is inverted for different angular positions on the rocking curve (Figs. 5*a* and 5*b*). The conventional synchrotron radiography of these samples was not shown here because they are almost transparent for this energy. The same procedure described above was used to simulate the cross-section profiles of the polyamide strands (shown in Fig. 6). The profiles of the images are non-symmetric because they were acquired at angular positions on the slope of the rocking curve (positions 2, 4 and 1 in Fig. 2, respectively). The profile would have been symmetric for an image acquired at the top angular position on the rocking curve (position 3 in Fig. 2).

The calculated profiles for all the samples did not agree well with the experimental results for several reasons. The samples did not have straight edges (Fig. 3), the analyzer crystal rocking curve was not a perfect Gaussian profile and the crystal was slightly bent, *i.e.* for large areas different parts of the sample are in different angular positions on the analyzer rocking curve. This was the main disadvantage of using an asymmetrical crystal set-up against the intrinsic advantage of the large field of view enabled with such a set-up. The strong difference found in the apparent absorption contrast cross-sectional profile between simulation and DEI algorithm (indicated in Fig. 4*e*) arises mainly due to the strains in the analyzer crystal (slightly bent). Another problem found in the simulations was near the edges of the samples owing to the high refraction angles and total external reflection in these regions. This really occurs but experimentally only a small part of the material (near the edge) deviates the X-rays at these higher angular values.
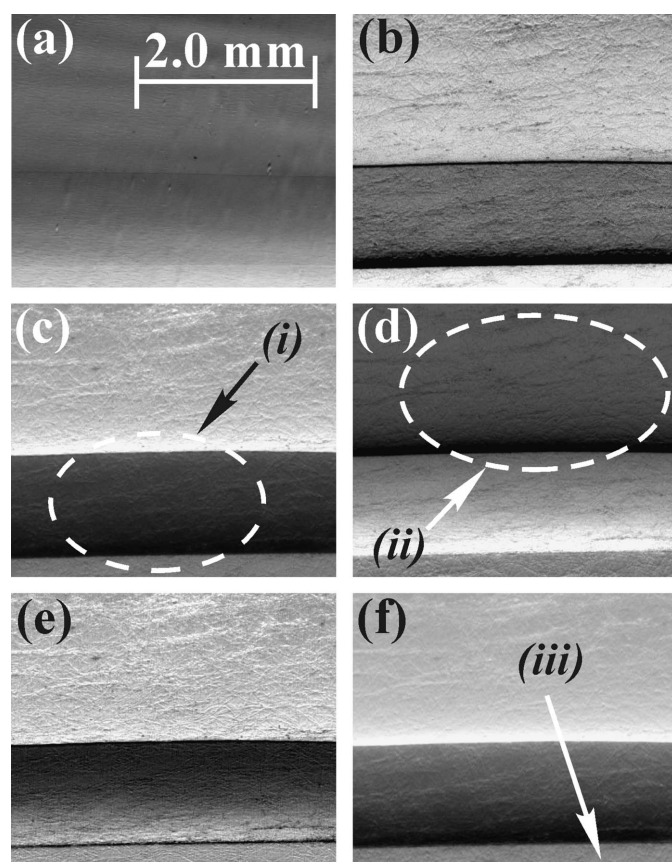
Figure 3
Images of the bottom half of the polypropylene tube. (*a*) Conventional synchrotron radiography; (*b*–*d*) ABIs at different angular positions on the rocking curve (positions 3, 2 and 5 in Fig. 2, respectively); (*e* and *f*) apparent absorption contrast and refraction angle images obtained using the DEI mathematical processing. Details indicated with arrows are (i) the tube wall, (ii) inside the tube and (iii) outside the tube.
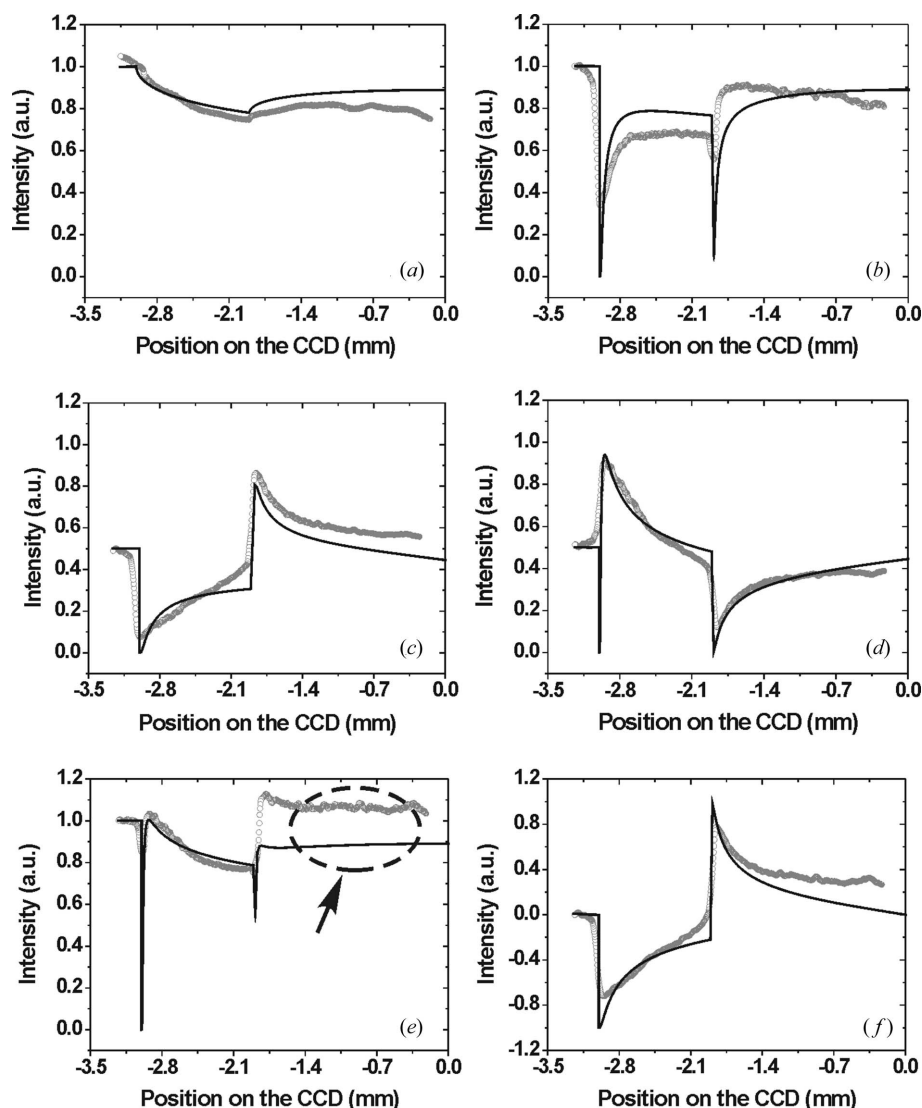
Figure 4
Measured (circles) and simulated (line) cross-sectional profiles of the images of Fig. 3. (*a*) Conventional synchrotron radiography; (*b*–*d*) ABIs at different angular positions on the rocking curve (positions 3, 2 and 5 as indicated in Fig. 2, respectively); (*e* and *f*) apparent absorption contrast and refraction angle cross-sectional profiles obtained with the DEI mathematical processing.
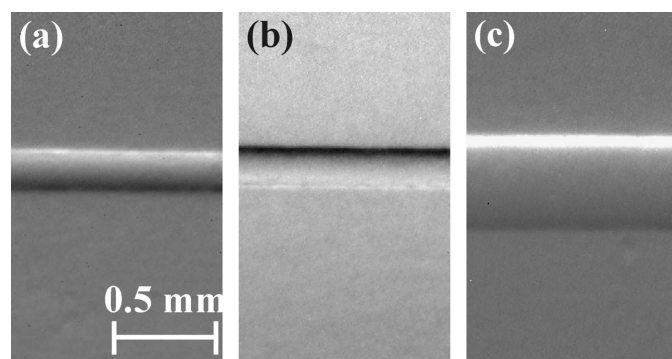
Figure 5
Images of the polyamide strands: (*a* and *b*) ABIs at different angular positions on the rocking curve (2 and 4 in Fig. 2, respectively) of the 100 µm-thick strand. (*c*) ABI obtained at the angular position (1) on the rocking curve (Fig. 2) of the 250 µm-thick strand.

The spatial resolution of this ABI system was also checked using a Cu 300 mesh. This was done by counting the number of pixels between two adjacent bright and dark details in the image acquired at the angular position at the top of the rocking curve. A spatial resolution of about 10 µm × 10 µm was measured and it was limited mainly by the point spread function of the CCD detector.

4. Qualitative studies

A slice of ox brain tissue and a violin spider were used as samples. The ox brain tissue was selected from the cortex of the frontal lobe. It was a 5 mm-thick sample of tissue embedded in Formol (a 36% solution of formaldehyde in water). With conventional synchrotron radiography, the ABI obtained at the top angular position on the rocking curve, the refraction angle and apparent absorption contrast images (DEI images) of the ox brain tissue are shown in Fig. 7. The contrast of the image of Fig. 7(*b*) (ABI) arises mainly from the refraction and extinction. This can be checked by comparing Figs. 7(*a*) (conventional synchrotron radiography), 7(*b*) and 7(*c*) (DEI images). Fig. 7(*c*) shows structures (contrast) arising from the spatial gradient of the refractive index while Fig. 7(*d*) shows contrast arising mainly from the extinction. The absorption contrast can be neglected in this last image because such structures cannot be seen in the conventional synchrotron radiography (Fig. 7*a*). Such structures are the sulcus and gyrus, respectively. The possibility of seeing details not shown with conventional synchrotron radiography in a sample of ox brain tissue could open the way to using this technique with other improved DEI algorithms (Rigon *et al.*, 2003; Pagot *et al.*, 2003; Oltulu *et al.*, 2003), possibly in conjunction with computed tomography (Dilmanian *et al.*, 2000; Wernick *et al.*, 2003), as a future auxiliary method for diagnosing brain diseases, not exploited here, like Alzheimer (Tanabe *et al.*, 1997), Creutzfeldt-Jacob disease and variant Creutzfeldt-Jacob disease (Almond & Pattison, 1997) in the earliest stages.

The PBI (edge detection geometry) and ABI (acquired on the top angular position of the rocking curve) of the *Loxosceles gaucho* spider are comparatively shown in Fig. 8. For the PBI (Fig. 8*a*) the sample was set downstream of the crystals with the detector positioned at a distance of 300 mm from the sample. Both PBI and ABI show a large quantity of detail but
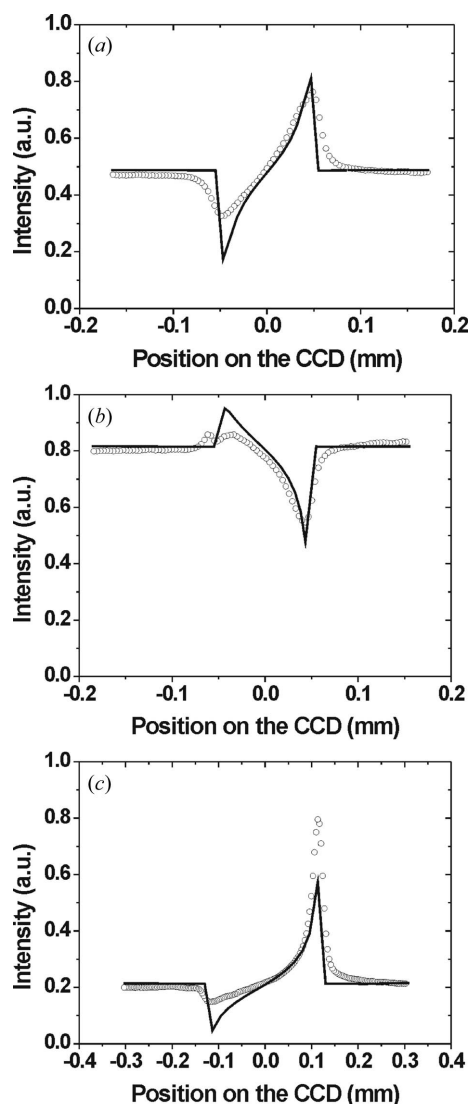
Figure 6
Measured (circles) and simulated (line) cross-sectional profiles of the images of Fig. 5. (*a* and *b*) ABIs at different angular positions on the rocking curve (2 and 4 in Fig. 2, respectively) of the 100 μm-thick wire. (*c*) ABI obtained at the angular position (1) on the rocking curve (Fig. 2) of the 250 μm-thick wire.

the contrast in the second one is higher. Some details of the spider anatomy are indicated in Fig. 8.

To avoid the problem of the strains in the analyzer crystal (slightly bent, as described in the previous section), for each angular position, the images were selected from an area on the CCD where the variations in the relative intensity of the flat field, *i.e.* the image without the sample, was less than 10%. This procedure had to be applied mainly to obtain reasonable DEIs. This problem with the asymmetrical crystal set-up can be solved by trying to manufacture large strain-free analyzer crystals.

5. Conclusions

An asymmetrical crystal set-up was mounted for quantitative and qualitative studies on analyzer-based X-ray phase contrast
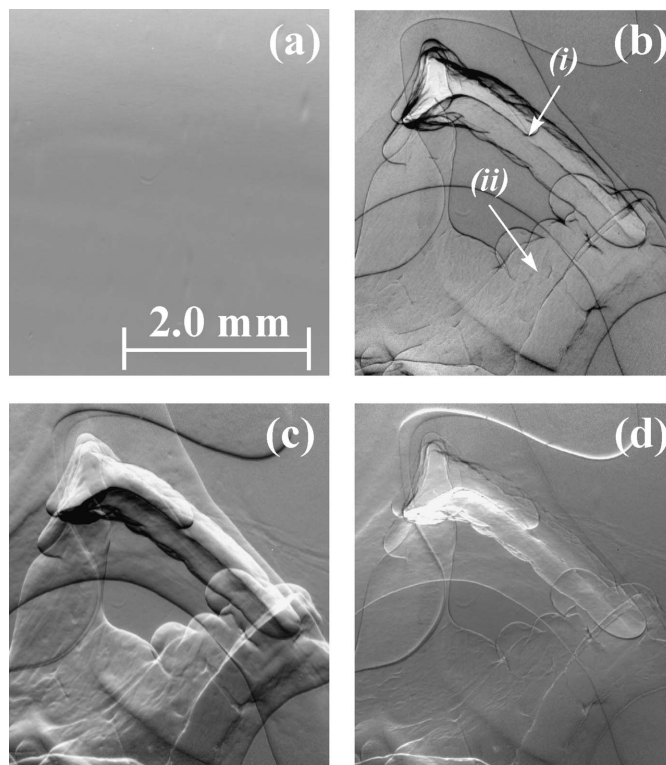
Figure 7
Images of the ox brain tissue: (*a*) conventional synchrotron radiography; (*b*) ABI at the angular position at the top of the rocking curve (position 3 in Fig. 2). (*c* and *d*) Refraction angle and apparent absorption contrast images obtained with the DEI mathematical processing. (i) and (ii) are the sulcus and gyrus, respectively.
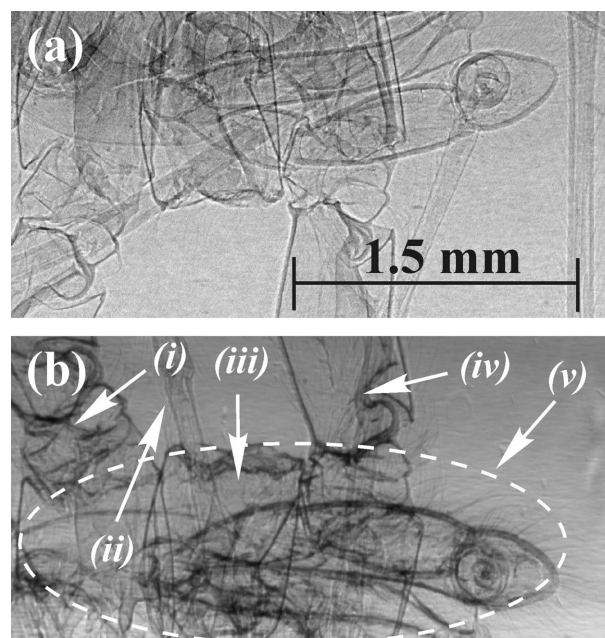
Figure 8
(*a*) PBI of the bottom half part of the violin spider (*Loxosceles gaucho*). (*b*) ABI of the top part of the same spider acquired at the angular position at the top of the rocking curve (position 3 in Fig. 2). (i) Leg 3, (ii) leg 4, (iii) part of leg 2 (iv) leg 1 and (v) encephalothorax.

imaging at the SYRMEP beamline of Elettra. The acquired images were also processed using the diffraction enhanced imaging algorithm. Measured and simulated cross-section profiles of the images of a polypropylene tube on a paper matrix and polyamide strands were shown. The agreement was not perfect with the experimental results because the samples did not have straight edges, the analyzer crystal was slightly bent and its rocking curve was not a perfect Gaussian profile. Also, another problem was found in the simulations, near the edges of the samples, owing to the high refraction angles and total external reflection in these regions.

Biological samples were also explored. A propagation-based X-ray phase contrast image of a *Loxosceles gaucho* spider (violin spider) was acquired and qualitatively compared with an ABI indicating that the latter provides higher contrast. Special attention was given to a 5 mm-thick sample of ox brain tissue, because this sample did not show any details in the conventional synchrotron radiography. In contrast, many details were found in the ABIs and DEIs. This could indicate that ABIs and DEIs with computerized tomography could be used in the future as an auxiliary method in diagnosing brain diseases like Alzheimer, Creutzfeldt-Jacob disease and variant Creutzfeldt-Jacob disease in the earliest stages.

References

Almond, J. & Pattison, J. (1997). *Nature (London)*, **389**, 437–438.

Ando, M. & Hosoya, S. (1972). *Proceedings of the 6th International Conference on X-ray Optics and Microanalysis*, edited by G. Shinoda *et al.*, p. 63. Tokyo: University of Tokyo.

Arfelli, F., Bravin, A., Barbiellini, G., Cantarore, G., Castelli, E., Di Michiel, M., Poropat, P., Rosei, R., Sessa, M., Vacchi, A., Dalla Palma, L., Longo, R., Bernstorff, S., Savoia, A. & Tromba, G. (1995). *Rev. Sci. Instrum.* **66**, 1325–1328.

Chapman, D., Thomlinson, W., Johnston, R. E., Washburn, D., Pisano, E., Gmür, N., Zhong, Z., Menk, R., Arfelli, F. & Sayers, D. (1997). *Phys. Med. Biol.* **42**, 2015–2025.

Cloetens, P., Pateyron-Salomé, M., Buffière, J. Y., Peix, G., Baruchel, J., Peyrin, F. & Schlenker, M. (1997). *J. Appl. Phys.* **81**, 5878–5886.

Coan, P., Pagot, E., Fiedler, S., Cloetens, P., Baruchel, J. & Bravin, A. (2005). *J. Synchrotron Rad.* **12**, 241–245.

Davis, T. J., Gao, D., Gureyev, T. E., Stevenson, A. W. & Wilkins, S. W. (1995). *Nature (London)*, **373**, 595–598.

Dilmanian, F. A., Zhong, Z., Ren, B., Wu, X. Y., Chapman, L. D., Orion, I. & Thomlinson, W. C. (2000). *Phys. Med. Biol.* **45**, 933–946.

Förster, E., Goetz, K. & Zaumseil, P. (1980). *Krist. Tech.* **15**, 937–945.

Hart, M. (1980). *Characterization of Crystal Growth Defects by X-ray Methods, NATO Advanced Study Institutes Series, Series B: Physics*, edited by B. K. Tanner and D. K. Bowen, p. 484. New York: Plenum.

Hönnicke, M. G., Kellerman, G., Rocha, H. S., Giles, C., Tirao, G., Mazzaro, I., Lopes, R. T. & Cusatis, C. (2005). *Rev. Sci. Instrum.* Submitted.

Ingal, V. N. & Beliaevskaya, E. A. (1995). *J. Phys. D*, **28**, 2314–2317.

Mannan, K. A., Arfelli, F., Beveridge, T., Butler, S., Chapman, D., Gillam, J., Hall, C., Juurlink, B., Kelly, K., Kelly, M., Lewis, R., McLoughlin, G., Menk, R., Pavlov, K., Pearson, S., Pillon, A., Rigon, L., Round, A., Schultke, E., Siu, K., Tromba, G., Wilkinson, S. & Griebel, R. W. (2005). *Nucl. Instrum. Methods A*. In the press.

Oltulu, O., Zhong, Z., Hasnah, M., Wernick, M. N. & Chapman, D. (2003). *J. Phys. D*, **36**, 2152–2156.

Pagot, E., Cloetens, P., Fiedler, S., Bravin, A., Coan, P., Baruchel, J., Härtwig, J. & Thomlinson, W. (2003). *Appl. Phys. Lett.* **82**, 3421–3423.

Pavlov, K. M., Gureyev, T. E., Paganin, D., Nesterets, Ya. I., Morgan, M. J. & Lewis, R. A. (2004). *J. Phys. D*, **37**, 2746–2750.

Podurets, K. M., Somenkov, V. A. & Shiåshtein, S. Sh. (1989). *Sov. Phys. Tech. Phys.* **34**, 654–657.

Protopopov, V. V. & Sobota, J. (2002). *Opt. Commun.* **213**, 4–6.

Rigley, S., Schultke, E., Ataelmannan, K., Chapman, D., Doucette, R., Griebel, R., Juurlink, B., Arfelli, F., Rigon, L., Menk, R., Tromba, G., Beveridge, T., Lewis, R., Pavlov, K., Siu, K. & Hall, C. (2005). *Nucl. Instrum. Methods A*. In the press.

Rigon, L., Besch, H.-J., Arfelli, F., Menk, R.-H., Heitner, G. & Plothow-Besch, H. (2003). *J. Phys. D*, **36**, A107–A112.

Snigirev, A., Snigireva, I., Kohn, V., Kuznetsov, S. & Schelokov, I. (1995). *Rev. Sci. Instrum.* **66**, 5486–5492.

Souvorov, A., Drakopoulos, M., Snigireva, I. & Snigirev, A. (1999). *J. Phys. D*, **32**, A184–A192.

Tanabe, J. L., Amend, D., Schuff, N., DiSclafani, V., Ezekiel, F., Norman, D., Fein, G. & Weiner, M. W. (1997). *Am. J. Neurorad.* **18**, 115–123.

Wernick, M. N., Wirjadi, O., Chapman, D., Zhong, Z., Galatsanos, N. P., Yang, Y., Brankov, J. G., Oltulu, O., Anastasio, M. A. & Muehleman, C. (2003). *Phys. Med. Biol.* **48**, 3875–3895.

Wilkins, S. W., Gureyev, T. E., Gao, D., Pogany, A. & Stevenson, A. W. (1996). *Nature (London)*, **384**, 335–338.

Zhong, Z., Thomlinson, W., Chapman, D. & Sayers, D. (2000). *Nucl. Instrum. Methods*, A**450**, 556–567.